Warm spraying—a novel coating process based on high-velocity impact of solid particles

2008 Sci. Technol. Adv. Mater. 9 033002

(http://iopscience.iop.org/1468-6996/9/3/033002)

IOP PUBLISHING SCIENCE AND TECHNOLOGY OF ADVANCED MATERIALS

Sci. Technol. Adv. Mater. **9** (2008) 033002 (17pp) doi:10.1088/1468-6996/9/3/033002

TOPICAL REVIEW

Warm spraying—a novel coating process based on high-velocity impact of solid particles

Seiji Kuroda[1], **Jin Kawakita**[1], **Makoto Watanabe**[1] **and Hiroshi Katanoda**[2]

[1] Composites and Coatings Center, National Institute for Materials Science, 1-2-1 Sengen, Tsukuba, Ibaraki 305-0047, Japan
[2] Department of Mechanical Engineering, Kagoshima University, Kagoshima 890-0065, Japan

E-mail: KURODA.Seiji@nims.go.jp

Received 28 January 2008
Accepted for publication 1 May 2008
Published 10 September 2008
Online at stacks.iop.org/STAM/9/033002

Abstract

In recent years, coating processes based on the impact of high-velocity solid particles such as cold spraying and aerosol deposition have been developed and attracting much industrial attention. A novel coating process called 'warm spraying' has been developed, in which coatings are formed by the high-velocity impact of solid powder particles heated to appropriate temperatures below the melting point of the powder material. The advantages of such process are as follows: (1) the critical velocity needed to form a coating can be significantly lowered by heating, (2) the degradation of feedstock powder such as oxidation can be significantly controlled compared with conventional thermal spraying where powder is molten, and (3) various coating structures can be realized from porous to dense ones by controlling the temperature and velocity of the particles. The principles and characteristics of this new process are discussed in light of other existing spray processes such as high-velocity oxy-fuel spraying and cold spraying. The gas dynamics of particle heating and acceleration by the spraying apparatus as well as the high-velocity impact phenomena of powder particles are discussed in detail. Several examples of depositing heat sensitive materials such as titanium, metallic glass, WC–Co cermet and polymers are described with potential industrial applications.

Keywords: thermal spray, coating, gas dynamics, high-velocity impact, titanium, metallic glass, WC–Co, titanium oxide, ultrahigh-molecular-weight polyethylene

(Some figures in this article are in colour only in the electronic version)

1. Introduction

The role of surface coatings has become increasingly important in industries because higher energy efficiency and longer service life are expected more strongly for various plants and structures. Thermal spraying holds a unique position in the spectra of surface modification technologies because it can provide thick coatings over 100 μm over a large area at a very high application rate compared with other coating processes such as electroplating, PVD and CVD [1]. Coating materials available for thermal spraying include metals, alloys, ceramics, plastics and composites. They are fed in powder or wire form, heated to a molten or semimolten state and accelerated towards substrates in the form of particles in the size range of several μm to 100 μm. Combustion or electrical arc discharge is usually used as the source of energy for thermal spraying and coatings are made by the accumulation of numerous sprayed particles.

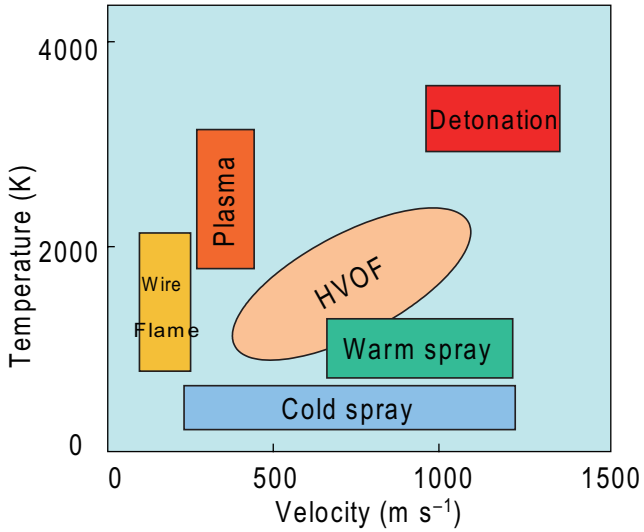

Figure 1. Comparison of various thermal spray processes in terms of particle temperature and velocity.

Figure 1 shows the classification of various thermal spray processes in terms of particle temperature and velocity. In classical but still widely used processes such as flame spraying and wire arc spraying, which were developed in the 1910s to the 1920s, the particle velocities are generally low below 150 m s^{-1}, and raw materials must be molten to be deposited. Plasma spraying developed in the 1970s uses a high-temperature plasma jet generated by arc discharge with typical temperatures of over 15 000 K, which makes it possible to spray refractory materials such as oxides and high melting-point metals such as molybdenum. During the 1980s, a class of thermal spray processes called high velocity oxy-fuel (HVOF) spraying was developed. Figure 2(a) shows a schematic of one type of commercial HVOF spray apparatus. A mixture of fuel and oxygen is fed into a combustion chamber, where they are ignited and combusted continuously. The resultant hot gas at a pressure close to 1 MPa emanates through a converging–diverging nozzle and travels through a straight section. The fuels can be gases such as hydrogen, methane, propane, propylene, acetylene and natural gas or liquids such as kerosene. The jet velocity at the exit of the barrel is usually over 1000 m s^{-1} and thus exceeds the velocity of sound. Powder material is fed into the jet at the feed ports and the powder particles are heated and accelerated toward the substrate, where they impinge at high velocity to form a coating. The process has been most successful for depositing cermet materials such as WC–Co and other corrosion-resistant alloys such as stainless steels and nickel-based alloys. A typical microstructure of 316L stainless steel coating is shown in figure 3(a), which clearly depicts that the coating contains both unmolten and molten particles. It is evident that larger particles tend to remain

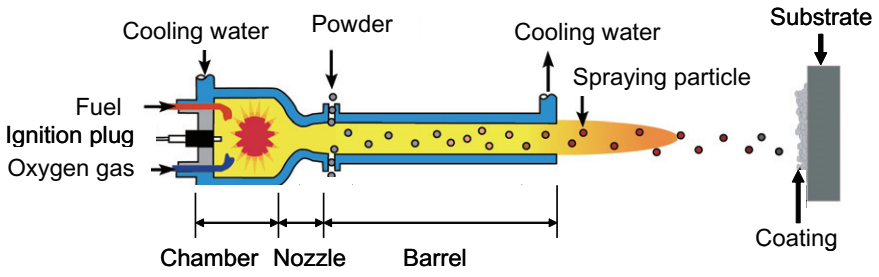

(a) High-velocity oxy fuel (HVOF) gun

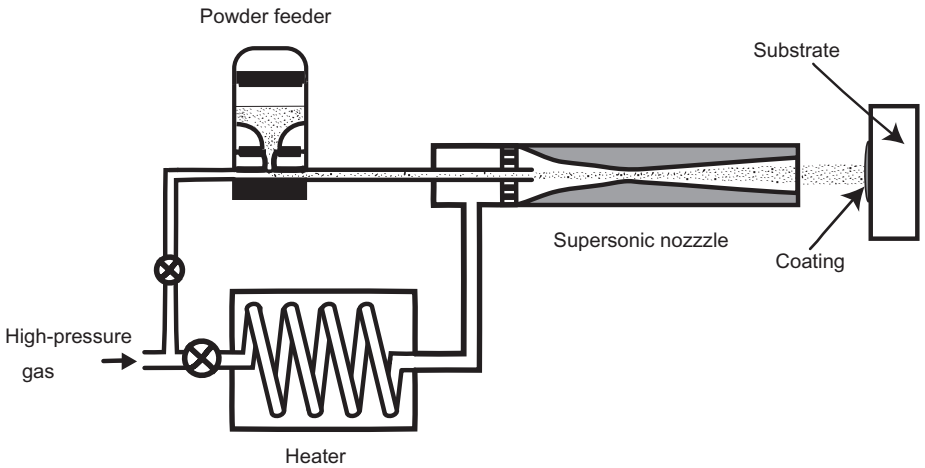

(b) Cold spray apparatus

Figure 2. Schematic of HVOF (a) and cold (b) sprayings.

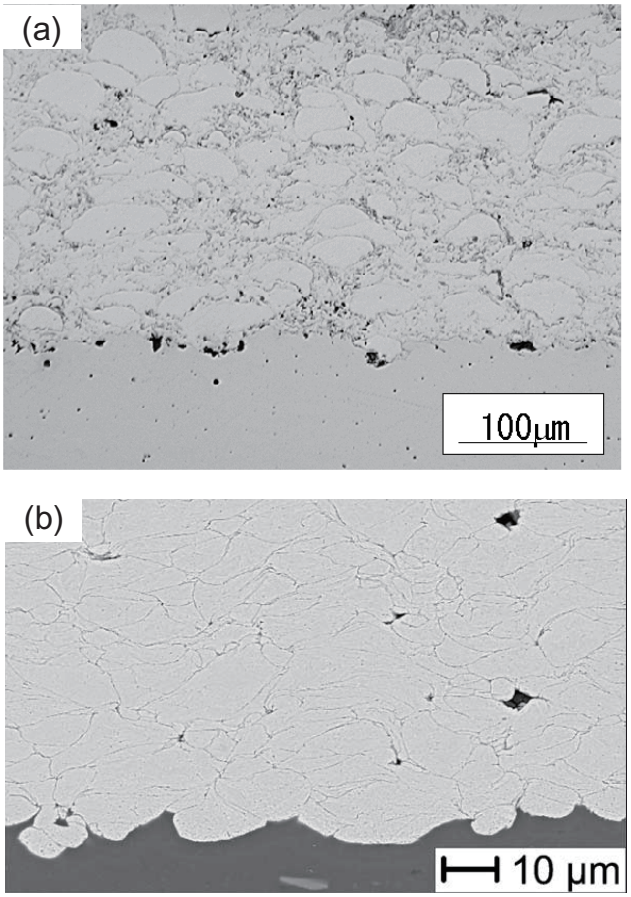

Figure 3. Typical microstructure of HVOF-sprayed 316L stainless steel coating (a) observed by optical microscopy and cold-sprayed copper (b) coating observed by scanning electron microscopy (backscattering mode). The latter sample was etched to reveal the article/particle boundaries (reproduced with permission from [18] ©2003 Elsevier Science Ltd).

unmolten owing to insufficient heat received during flight. In the 1990s, cold spraying (often called cold gas dynamic spraying) was introduced into the thermal spray market [2]. The method was originally developed in Russia with the accidental observation of the rapid formation of coatings, while experimenting the particle erosion of the target surface exposed to a two-phase flow of high velocity loaded with fine powder in a wind tunnel. As shown in figure 2(b), the main elements of the cold spray setup are the spraying unit consisting of a prechamber and a supersonic nozzle, the powder feeder, the gas heater and the source of compressed gas. Particles are accelerated to very high speeds by the carrier gas forced through a converging–diverging de Laval type nozzle. Upon impact, solid particles with sufficient kinetic energy deform plastically and bond mechanically to the substrate to form a coating. As will be explained in detail in section 4, the critical velocity needed to form bonding depends on the material's properties, powder size and temperature. Soft metals such as copper and aluminum are best suited for cold spraying, as shown in figure 3(b); however, the coating formation of other materials such as tungsten, tantalum, titanium, MCrAlY and WC–Co by cold spraying has been reported. However, the deposition efficiency tends to be low, and the window of process parameters and suitable powder size distribution tend do be narrow. To accelerate powders to higher velocity, finer powders below 20 μm are usually used. As processing gas, it is possible to accelerate powder particles to a significantly higher velocity using helium than using nitrogen owing to its high velocity of sound; however, helium is much more costly and its flow rate tends to be greater. To improve acceleration capability, nitrogen gas is heated to a higher temperature and the maximum gas temperature realized in cold spraying today appears to be approximately 1173 K [3]. As a merit of heating the process gas, significant increases in the deposition efficiency and tensile strength of copper deposits were reported.

Another approach taken by the authors is to lower the temperature of combustion gas generated in high-velocity oxy-fuel spraying. As will be described in the next section, by mixing nitrogen with a combustion gas, it is possible to operate in the gas temperature range between HVOF and cold spraying. Even though the gas generated contains significant amount of water vapor, unreacted hydrocarbon and oxygen, and thus is not as clean as the gas used for cold spraying, the reaction of powder with the gas is relatively mild because the powder material remains unmolten during spraying as will be demonstrated for titanium in the following section. Since the process operates in the intermediate temperature range between HVOF spraying and cold spraying, it was given the name 'warm spraying'; it is considered to have certain advantages and disadvantages over these processes.

2. Process description of warm spraying and numerical analysis of titanium powder in flight

2.1. Gas dynamics of warm spraying

A common feature of all thermal spray processes is that particles that form a coating are heated and accelerated toward the substrate. This is achieved by feeding powder into the high-velocity stream of gas or by generating paritlces *in situ* through the disintegration of wires from the tip as a result of heating from the arc discharge or high-temperature gas stream. From the viewpoint of coating formation, it is very important to know the size, temperature and velocity distribution of the flux of the particles impinging onto the substrate as they determine the deposition efficiency of the process and the microstructure of the coatings.

There are several diagnostic devices for measuring the temperature and velocity of sprayed particles. The velocity can be measured using a Doppler anemometer. Temperature measurement is more difficult but a high-speed two-color pyrometer has been commercialized, which is reliable for oxides but not very reliable for metals possibly because of the change in the spectral emittance of the surface, which is highly sensitive to the formation of thin surface oxides.

Another useful approach is numerical simulation because it can analyze flow fields and particle behavior inside the spraying apparatus, thereby saving much of the time and cost needed for experiments.

Figure 4 shows the schematic of the warm spraying process, which is modified from commercial HVOF spraying

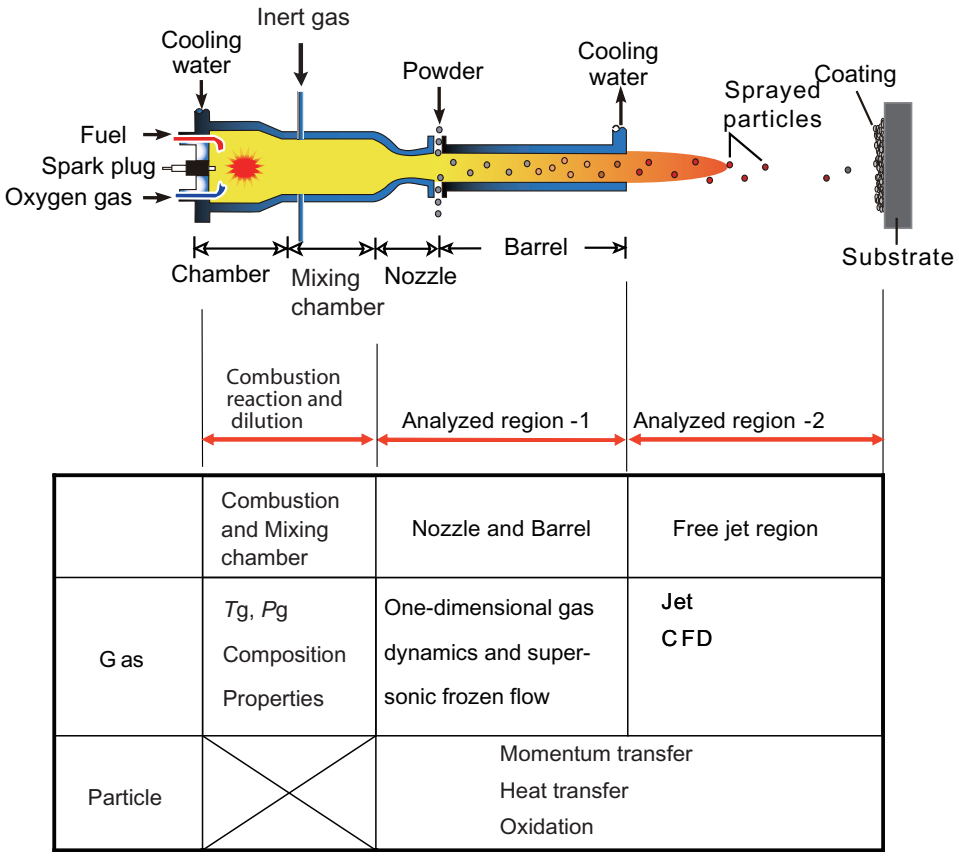

Figure 4. Schematic of two-stage HVOF (warm spraying) process with table showing classification of regions for mathematical modeling.

Table 1. List of typical operating conditions in warm spraying. Flow rates of kerosene, oxygen and nitrogen.

Kerosene (slm)	Oxygen (slm)	Nitrogen (slm)
0.35	732	500
0.33	643	1000
0.30	623	1500
0.29	548	2000

slm, standard liter min^{-1}.

equipment. A mixture of kerosene and oxygen is combusted continuously to generate a hot gas, into which nitrogen gas is injected inside the mixing chamber inserted between the combustion chamber and the converging–diverging nozzle. By adjusting the flow rate of the nitrogen gas injected into the HVOF system, the flame temperature and concentrations of the gas species can be controlled. Table 1 lists a typical set of operating conditions. The mixing ratio of kerosene to oxygen is set at the stoichiometric ratio for complete combustion. The flow rates of kerosene and oxygen had to be reduced as nitrogen flow rate increased owing to the increase in the pressure within the combustion chamber. A quasi-one-dimensional gas dynamics model is used for the region inside the spray apparatus, which starts from the combustion chamber to the exit of the barrel. Outside the barrel, semiempirical equations are used to calculate the gas velocity and temperature of the gas jet.

The modeling involves two parts: the simulation of the gas/particle flow field characteristics inside and outside the spray gun, and the calculation of the incremental mass gain by the oxidation of particles based on the particle flow field characteristics obtained in the first section.

2.1.1 Combustion and mixing of nitrogen. To estimate the composition and temperature of the gas in the mixing chamber, the following simplified reaction is assumed for kerosene combustion in the combustion chamber followed by mixing with nitrogen in the mixing chamber:

$$\begin{aligned} C_{10}H_{20} + \nu_{O_2}O_2 + \nu_{N_2}N_2 \quad &\rightarrow 10(1-\xi)CO_2 + 10\xi CO \\ &+(5\xi + \nu_{O_2} - 15)O_2 + 10H_2O + \nu_{N_2}N_2. \end{aligned} \tag{1}$$

Here, ν_{O_2} and ν_{N_2} are determined by the operating conditions in table 1, and ξ reflects the degree of incomplete combustion. In order to determine ξ, gas sampled from the powder feed ports were analyzed using a gas analyzer (XPO-318, New Cosmos Electric Co., Ltd, Osaka, Japan). On the basis of the composition of the gas and temperature, various thermophysical properties of the gas such as specific heat, density, thermal conductivity and viscosity were calculated.

2.1.2 Gas and paticle flow fields. The gas velocity and temperature field from the nozzle to the barrel exit was calculated by integrating equations (2) to (5) [4, 5], which take account of the change in the cross-sectional area of

gun A, the friction in the barrel, and the heat loss to the cooling water through the inner wall of the barrel. The heat loss to the cooling water was determined experimentally by measuring the flow rates and temperatures of the water at the inlet and outlet of the apparatus. The heat loss to the cooling water was varied from 80 to 110 kW depending on the operating conditions, whereas the total power generated by the combustion was fixed at approximately 200 kW.

$$\frac{\mathrm{d}u_\mathrm{g}}{\mathrm{d}x} = \frac{u_\mathrm{g}}{(M_\mathrm{g}^2-1)}\frac{\mathrm{d}A}{A\mathrm{d}x} - \frac{u_\mathrm{g}}{(M_\mathrm{g}^2-1)}\left(\frac{\gamma M_\mathrm{g}^2}{2}\frac{4f}{\mathrm{d}} - \frac{\gamma-1}{\gamma R T_\mathrm{g}}\frac{\delta q}{\mathrm{d}x}\right), \tag{2}$$

$$\frac{\mathrm{d}\rho_\mathrm{g}}{\mathrm{d}x} = -\rho_\mathrm{g}\left(\frac{1}{u_g}\frac{\mathrm{d}u_\mathrm{g}}{\mathrm{d}x} + \frac{1}{A}\frac{\mathrm{d}A}{\mathrm{d}x}\right), \tag{3}$$

$$\frac{\mathrm{d}T_\mathrm{g}}{\mathrm{d}x} = \frac{\gamma-1}{\gamma R}\left(-\frac{\delta q}{\mathrm{d}x} - u_\mathrm{g}\frac{\mathrm{d}u_\mathrm{g}}{\mathrm{d}x}\right), \tag{4}$$

$$p = \rho_\mathrm{g} R T_\mathrm{g}, \tag{5}$$

where u_g: gas velocity; M_g: gas Mach number; A: cross sectional area; γ: specific heat ratio; f: friction factor; d: barrel diameter; R: gas constant; q: heat loss per unit mass of gas; ρ_g: gas density; T_g: gas temperature; p: static pressure.

Semiempirical equations [6] were used to calculate the gas velocity and temperature along the center line outside the barrel. The under- and over-expansions of the jet flow were also modeled as stepwise changes in the gas velocity and temperature at the barrel exit by introducing a fully expanded jet Mach number [7], as will be shown later in figures 5(a) and (b). The gas velocity and temperature in the potential-core [8] region of the jet were set at constant values, which are calculated using a fully expanded jet Mach number.

Once the gas flow field $u_\mathrm{g}(x)$ and $T_\mathrm{g}(x)$ are obtained, the acceleration and heating of a titanium spherical particle injected at the powder feed port can be, respectively, expressed by equations (6) and (7), and the velocity and temperature of one particle along the center line are obtained by integrating these equations [4, 6]:

$$m_\mathrm{p}\frac{\mathrm{d}u_\mathrm{p}}{\mathrm{d}t} = \tfrac{1}{2}C_\mathrm{d}\rho_\mathrm{g}\left(u_\mathrm{g}-u_\mathrm{p}\right)\left|u_\mathrm{g}-u_\mathrm{p}\right|\cdot\tfrac{\pi}{4}d_\mathrm{p}^2, \tag{6}$$

$$m_\mathrm{p}C_\mathrm{p}\frac{\mathrm{d}T_\mathrm{p}}{\mathrm{d}t} = \alpha\left(T_\mathrm{g}-T_\mathrm{p}\right)\cdot\pi d_\mathrm{p}^2, \tag{7}$$

$$\alpha = \frac{N_\mathrm{u}k_\mathrm{g}}{\mathrm{d_p}}, \tag{8}$$

$$Nu = 2 + 0.6Re^{0.5}Pr^{0.33}, \tag{9}$$

where m_p: particle mass; u_p: particle velocity; C_d: drag coefficient; d_p: particle diameter; C_p: specific heat of particle; T_p: particle temperature; Nu: Nusselt number; k_g: gas thermal conductivity; Re: Reynolds number; Pr: Prandtle number.

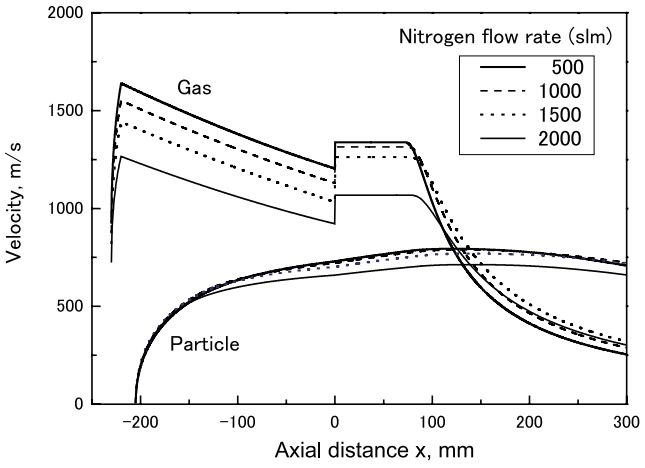

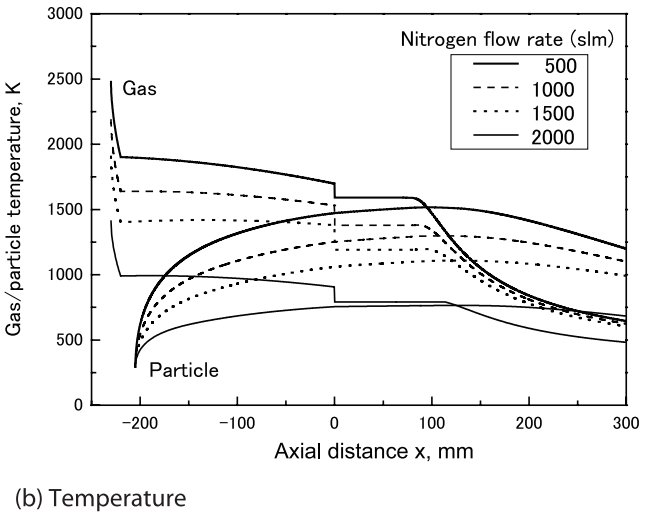

Figure 5. Gas and particle velocity profiles (a) and temperature profiles (b) starting from exit of nozzle. Axial distance $x = 0$ denotes the exit of the barrel.

2.1.3 Model results. Figure 5(a) shows the calculated gas velocity and velocity of a 30-μm-diameter titanium powder injected at the powder feed port. Here, the distance $x = 0$ corresponds to the barrel exit of the nozzle and the powder feed ports are located approximately 200 mm upstream. As the gas expands through the nozzle, its velocity increases rapidly and then decreases gradually along the barrel length due to friction with the inner wall of the barrel. Outside the barrel, the gas velocity increases stepwise, which represents the underexpansion of the jet flow at the barrel exit, and remains constant in the potential-core region outside the barrel, and then decreases again owing to mixing with the ambient air. Note that the gas velocity is higher with a lower nitrogen flow rate through the gun and the potential-core region of the jet. This is mainly due to the higher gas temperatures in the barrel and jet. It is very interesting to see that the velocity profiles of the Ti particle are almost unaffected by the nitrogen flow rate. This is attributed to the increase in the gas density with the addition of nitrogen, which compensated for the decreased gas velocity.

Figure 5(b) shows the significant effect of mixing nitrogen on the temperatures of the mixed gas and particles. The gas temperature steeply decreases owing to the expansion of the gas through the nozzle and then gradually decreases owing to the heat loss to the water-cooled barrel, remains constant in the potential-core region of the jet, and then decreases again owing to mixing with ambient air. In summary, the numerical simulation shows that the particle temperature at the barrel exit can be changed from 1500 to 600 K, while keeping particle velocity relatively unchanged. Even at distances of 200 and 300 mm downstream of the barrel, where the substrates are placed, this tendency generally remains.

2.2. Oxidation of titanium particles [9]

Recent studies of the oxidation of molten thermal sprayed particles revealed that the internal flow within the particles induced by the aerodynamic shear at the droplet surface can markedly increase the extent of in-flight oxidation by promoting the entrapment of surface oxides within the molten droplet and by continually exposing fresh fluid available for oxidation [10, 11]. In plasma spraying, vaporization needs to be considered in some cases. When the oxides formed are volatile, the vaporization of the oxides may reduce the amount of oxides trapped in the final coatings.

In warm spraying, however, the situation is much simpler as the particles never reach the melting point; thus it is expected that the oxidation rate is much lower than that in processes where the particles are molten. As compared with cold spraying, where only inert gas is used such as nitrogen or helium, it is expected that warm spraying should cause more pronounced oxidation but the difference should be evaluated carefully as the substrate in cold spraying is placed in air.

In the following, a numerical simulation of the oxidation of titanium particles in warm spraying is briefly described, and its results are compared with experimental results. Even though the parameters used for the modeling of titanium, which is one of the metals most reactive with oxygen, were cited from the literature on the basis of the experiments on isothermal oxidation in pure oxygen atmosphere, the effect of oxygen partial pressure on the oxidation kinetics of titanium was shown to be negligible down to 1 Pa [12]. The measurement of oxygen concentration in the combustion gas showed that the partical pressure of oxygen inside the spraying gun is at a level much higher than this [9].

Results of the particle temperature and velocity profiles were incorporated into the oxidation model. Then, the oxidation model was used to calculate the mass gain per unit surface area on the basis of the experimental parabolic rate constants obtained from published isothermal measurements [13]. It is well-documented that at the initial stage of oxidation, titanium conforms to the parabolic rate law in the temperature range of 327–1377 °C. Also, it was suggested that the oxidation involves two processes: the formation of new oxide layers, by the migration of anion vacancies generated at the oxide/metal interface, and the dissolution of interstitial oxygen atoms into the metal. The

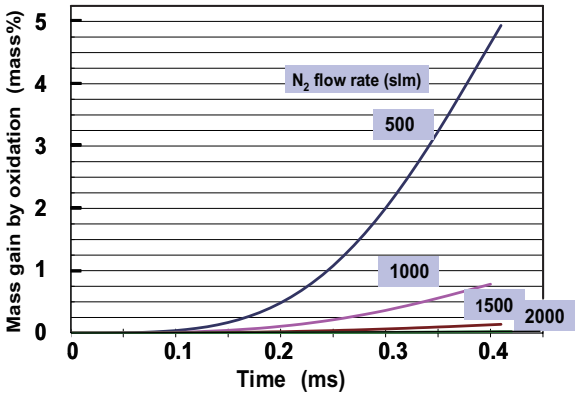

Figure 6. Mass gain due to in-flight oxidation of 30-mm-diameter titanium powder particles injected from powder injection port to barrel exit point.

rates of these two processes also follow the parabolic rate laws, and the associated parabolic rate constants were denoted k_s and k_m for the formation of oxides and the dissolution of interstitial oxygen, respectively. Equations (10)–(13) express the mass gain ΔW_{ox} as a function of time [9].

$$\Delta W_{ox} = k\sqrt{t}, \tag{10}$$

$$k = k_s + k_m, \tag{11}$$

$$k_s = k_{o,s} \exp(-E_s/RT), \tag{12}$$

$$k_m = k_{o,m} \exp(-E_m/RT). \tag{13}$$

The overall parabolic rate constant k can be expressed as the sum of the two constants shown in equation (11). The frequency factors ($k_{o,s}$ and $k_{m,s}$) and the activation energies (E_s and E_m) were determined on the basis of the fitting of the published experimental values of k over $1/T$ using equation (11).

Unlike in the isothermal oxidation experiment, particle temperature changes continuously starting from the moment of powder injection. The mass gain of each particle in each time step (Δt) is calculated from the parabolic rate constant $k(T(t))$ at the temperature $T(t)$ and the mass gain up to that time $\Delta W_{ox}(t)$, which together give the slope of the parabolic mass gain curve at the temperature and accumulated mass gain.

The calculated mass gains due to oxidation as a function of particle flight time for nitrogen flow rates of 500, 1000, 1500 and 2000 slm were calculated for a particle size of 30 μm, as shown in figure 6. Since the particle velocities at this particle size are almost the same for the four nitrogen flow rates (figure 5), the flight times within the barrel are almost the same at 0.4 ms. However, the overall mass gain at 500 slm was much higher than those at 1000 and 1500 slm, which coincide with the experimental results previously reported. The higher oxidation rate at 500 slm was caused by the exponential increase in the parabolic rate constant over 900 K. Beyond

Table 2. Comparison of measured oxygen content in warm sprayed titanium coatings with calculation. Calculated mass gain was added to the oxygen content of the feedstock powder (0.141%).

Oxygen	Nitrogen flow rate (slm)			
content (mass%)	2000	1500	1000	500
Expt.	0.22	0.25	1.30	5.30
Calc.	0.16	0.28	0.93	5.08

this temperature, the extent of overall oxidation increases significantly, and the oxidation becomes predominated by the oxygen dissolution in the metal [12]. The calculated oxygen content is compared with the experimental values in table 2. The calculated values tended to be smaller than those obtained from the coatings, which should be attributed to the in-flight oxidation in the region between the barrel exit and the substrate and oxidation on the substrate after deposition.

The oxygen contents of the coatings analyzed by the inert gas fusion method decreased significantly from 5.5 to 1.5 mass% when the nitrogen flow rate increased from 500 to 1000 slm at the same stand-off distance of 280 mm. The decrease in the oxygen content is caused by the lower flame temperature. At a flow rate of 2000 slm, the oxygen content decreased further to 0.22 mass%. Since titanium is one of the metals most reactive with oxygen, the results shown here indicate that oxidation can be significantly controlled under the condition that the particle velocity exceeds the critical velocity of titanium for forming bonds while heating the titanium particle over 1000 K.

3. Particle impact in warm spraying

In warm spraying, a feedstock particle is moderately heated and impacts on a substrate in the solid state, as discussed in the previous section. In this section, the bonding mechanism of a solid-state particle is discussed, which is becoming one of the most important research topics for processes based on the high-velocity impact of solid particles such as warm spraying and cold spraying.

3.1. Possible bonding mechanisms

Various phenomena of the impact of a particle on a solid substrate can be observed depending on particle size and impact velocity. Klinkov *et al* [14] described the schematic classification map of such phenomena. Figure 7 was obtained by modifying figure 1 in the reference to highlight the region of warm spray deposition. According to the figure, small particles ($d_p \approx 0.1$–$1.0\,\mu$m) can stick to the surface after impact at low particle velocities ($v_p \approx 1$–$100\,\mathrm{m\,s^{-1}}$) by van der Waals and electrostatic forces. For larger particles ($d_p \approx 5$–$150\,\mu$m), at moderate and low impact velocities ($v_p \approx 5$–$300\,\mathrm{m\,s^{-1}}$), impacted particles can rebound and repeated impacts on the same part of a substrate cause the deformation and destruction of the surface, that is, erosion. At higher particle velocities ($v_p \approx 300$–$1200\,\mathrm{m\,s^{-1}}$), particles can form a strong bonding with the surface after impact. With further increase in particle velocity ($v_p > 1000$–$3000\,\mathrm{m\,s^{-1}}$),

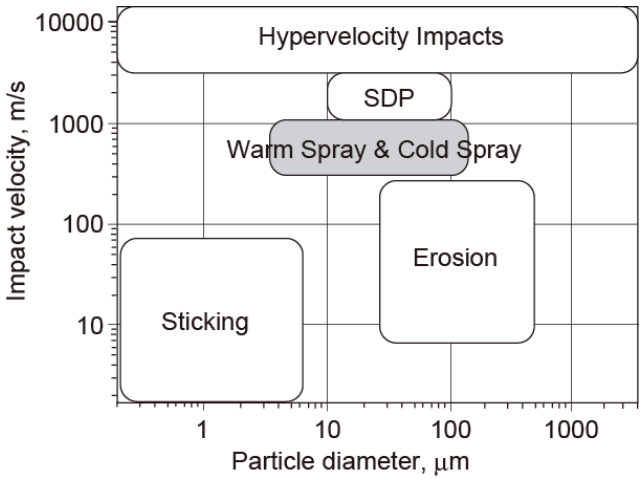

Figure 7. Classification map of phenomena for solid particle impact on solid surface in terms of impact velocity and particle diameter. This figure is made by modifying figure 1 in [14].

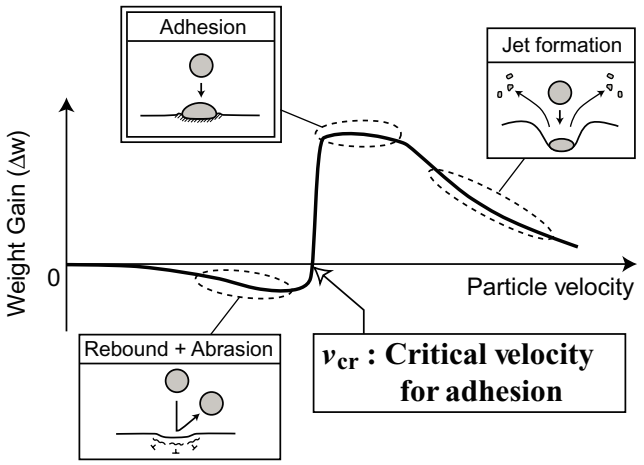

Figure 8. Concepts of critical velocity.

some hard particles show super-deep penetration (SDP) into the substrate with depths of about 10^3–10^4 diameters of the particles depending on the combination of the particle and the substrate. At impact velocities greater than 2000–3000 $\mathrm{m\,s^{-1}}$, stresses arising in bodies from impact significantly exceed the yield point of materials and materials behave like liquids.

Warm spray deposition usually utilizes particles with a diameter of $d_p \approx 5$–$100\,\mu$m corresponding to the region 'warm spray and cold spray' in figure 7. Understanding the adhesion mechanisms of particles to the substrate surface is a key problem in the development of new coatings for such a spray deposition technique. It is generally accepted by various experimental results that there exists a critical velocity, which the particle velocity has to exceed in order to successfully obtain a coating, as shown in figure 8 [15–19]. When the particle velocity is low, the particle rebounds on the surface upon impact. As the velocity increases, the particle starts to erode the substrate surface resulting in a weight loss of the substrate materials. When the velocity reaches its characteristic value, the particle starts to adhere on the surface. This velocity is called the critical velocity. If the particle

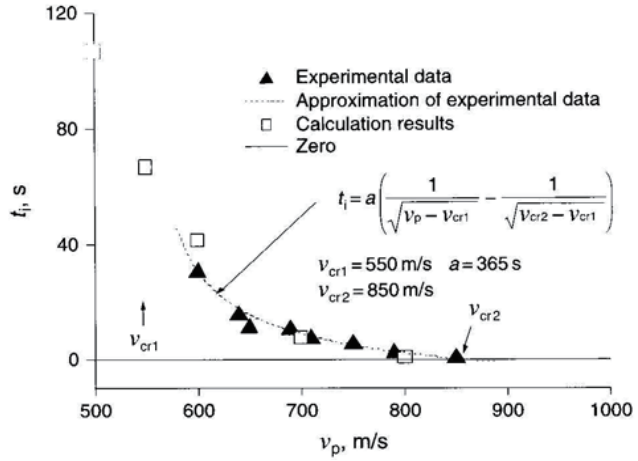

Figure 9. Incubation time results versus mean impact velocity of aluminum particles on polished copper substrate (reproduced with permission from [2] ©2007 Elsevier Science Ltd).

velocity further increases, hypervelocity impact phenomena start to show up with noticeable jet formation and significant weight loss. Critical velocity depends on sprayed materials and is very important for spray techniques based on the impact of solid particles.

Grujicic *et al* [20] cited three bonding mechanisms for solid particle impacts, namely, (i) atomic diffusion, (ii) surface adhesion, and (iii) plastic deformation, and argued their adequacy. As regards atomic diffusion in the case of the impact between aluminum and copper, since the interdiffusion coefficients of Cu-Al are 10^{-15}–$10^{-14}\,m^2\,s^{-1}$, the atomic interdiffusion distances are only 0.004–0.1 nm during a time period of ∼20 ns, over which the particle/substrate interface is subjected to the highest temperatures. This very small interdiffusion distance implies that the atomic diffusion is not a predominant bonding mechanism for cold spraying.

As regards surface adhesion, Alkimov *et al* [14, 21] reported that the deposition of particles is only observed after a certain incubation time has passed. Figure 9 shows a typical experimental dependence of incubation time as a function of particle-impact velocity and an approximation curve of the incubation time for aluminum particles with a mean diameter of 30.2 μm on a polished copper substrate [21]. When the particle velocity is lower, a longer incubation time is necessary for bonding and when the velocity reaches a specific value (v_{cr2}), the particles starts to adhere upon first impact. They also pointed out that particles do not adhere to the surface regardless of the time of treatment at an impact velocity lower than v_{cr1}. This indicates that the first impinging particles increase the chemical activity of the surface owing to the induction of an elevated concentration of dislocations in the superficial layer and the breakup of a very thin oxide layer on the substrate surface. Li *et al* [22] reported a very high deposition efficiency for titanium compared with that predicted by the plastic deformation model (more precisely a shear instability bonding criterion model) and pointed out the importance of metal reactivity and oxide films on particle surfaces.

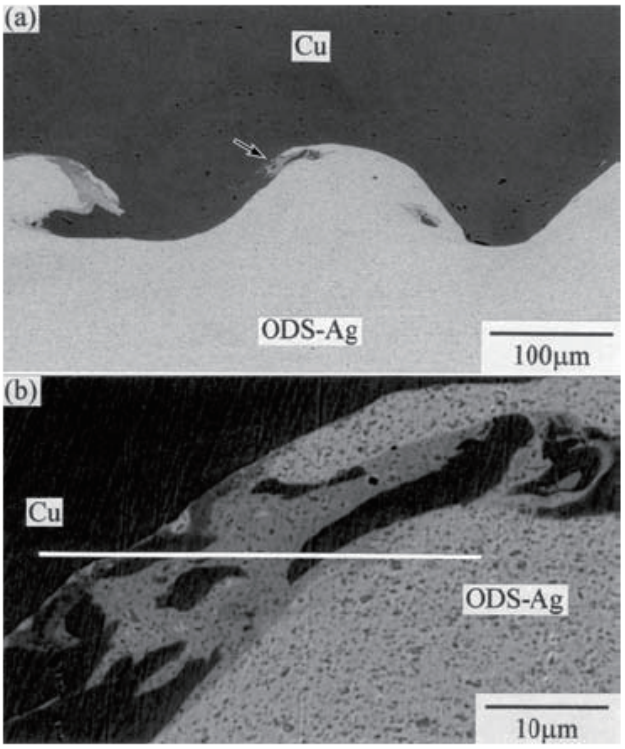

Figure 10. Wavy and vertical interfaces at explosive cladding of Cu and ODS-Ag (reproduced with permission from [23] ©2005 Japan Welding Society).

As regards plastic deformation, high contact pressure upon impact causes interfacial perturbations (roll-ups and vortices) that can give rise to nano-micro-scale material mixing and mechanical interlocking. In the case of explosive cladding, the formation of a wavy or vertical interface is often observed, as shown in figure 10 [23], and the main bonding mechanisms are considered as adiabatic welding [24]. This bonding is characterized by adiabatic shear instability and jet formation at the welding interface. Borchers *et al* [24] found a very thin copper layer (∼100 nm) with a low dislocation density at the interface of copper particles sprayed by cold spray deposition. According to them, these microstructures are possibly the results of the formation of jet at the interface.

3.2. Numerical analyses of solid particle impact

Numerical analyses have been carried out in order to simulate solid particle impact behaviors focusing on critical velocity. Assadi *et al* [18] calculated the deformation of both the particle and the substrate, together with the resultant strain and temperature distribution as functions of time under adiabatic condition by dynamic analysis using FEM. Critical velocity was determined as the velocity at which a shear instability begins at the interface by monitoring the plastic strain at the critical node of a particle. On the basis of their calculations, the following simple formula for estimating the critical velocity v_{cr} was proposed:

$$v_{cr} = 667 - 14\rho + 0.08T_m + 0.1\sigma_u - 0.4T_i, \qquad (14)$$

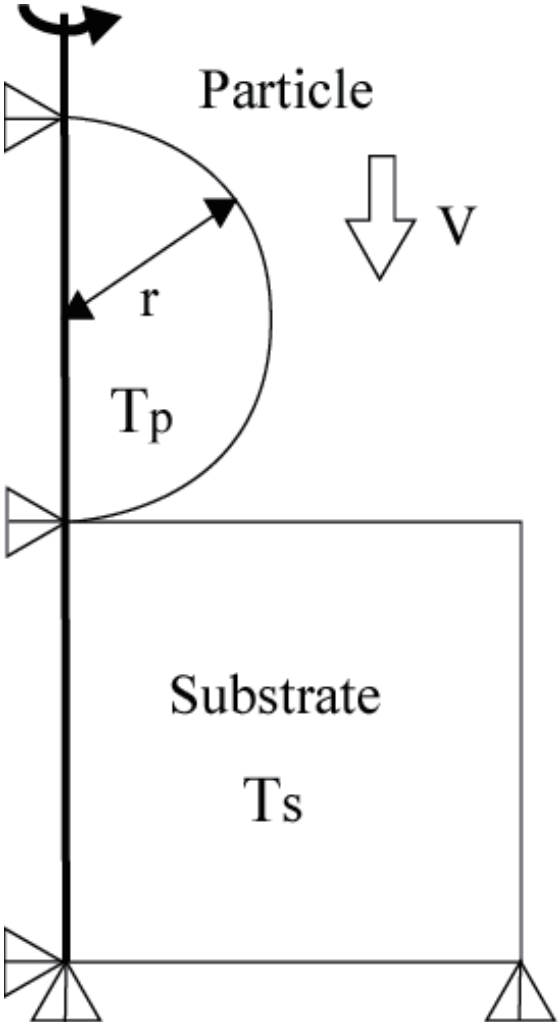

Figure 11. Schematic of numerical calculations (reproduced with permission from [26] ©2006 Japan Thermal Spraying Society).

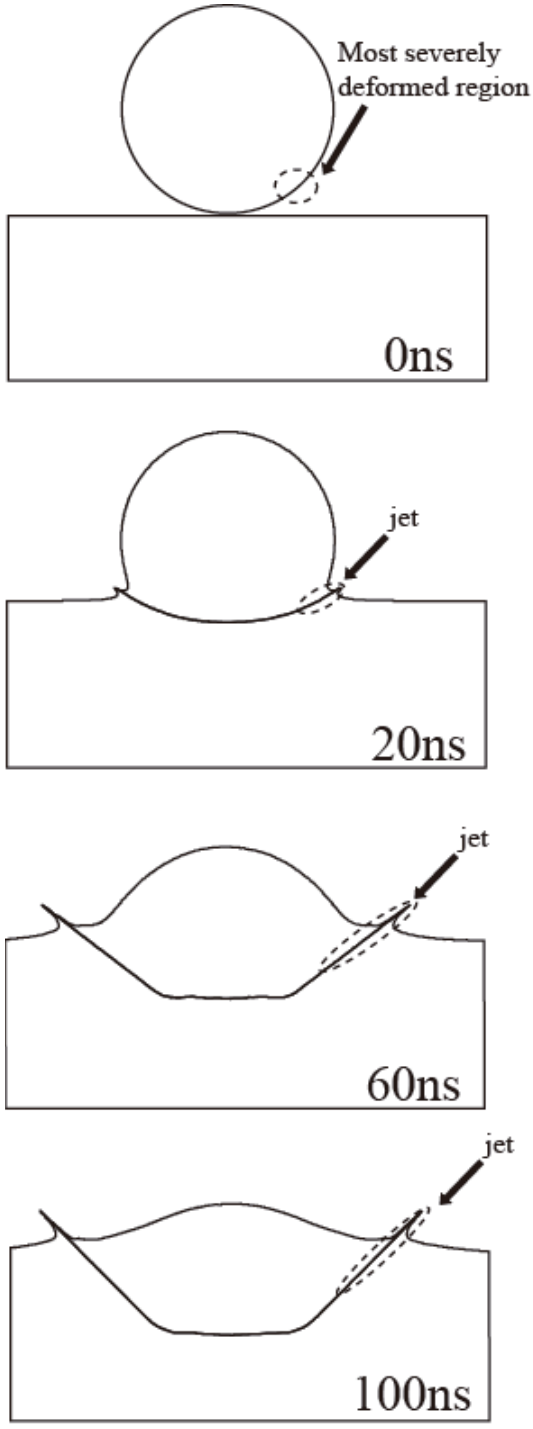

Figure 12. Sequence of copper particle deformation during impact simulated for $r = 50\,\mathrm{mm}$, $T_\mathrm{p} = 293\,\mathrm{K}$ and $V_\mathrm{p} = 550\,\mathrm{m\,s^{-1}}$ showing formation of jet at interface (reproduced with permission from [26] ©2006 Japan Thermal Spraying Society).

where ρ is the density in $\mathrm{g\,cm^{-3}}$, T_m is the melting temperature in °C, σ_u is the ultimate strength in MPa and T_i is the initial particle temperature in °C. Schmidt *et al* [25] extended Assadi *et al*'s model and discussed the effect of particle size on bonding criteria by taking into account heat conduction at the interface. In addition, by considering the condition to cause erosion as the particle velocity increases excessively, they proposed the concept of the 'window of sprayability' in terms of particle velocity, particle temperature and particle size.

The schematic of the typical single particle impact simulation model is shown in figure 11. Figure 12 shows the sequence of the deformation of a copper particle impacted onto a substrate for a particle diameter of 50 μm, a particle initial temperature of 293 K, and an initial velocity of $550\,\mathrm{m\,s^{-1}}$ calculated by Yokoyama *et al* [26]. The material parameters used in this calculation are listed in table 3. In the simulation, an axis symmetric model was used. A particle with a radius r impacts on the substrate. T_p and T_s are the temperatures of the particle and substrate, respectively. The Johnson–Cook plastic deformation model was applied and an adiabatic process (no heat transfer) was assumed throughout the calculation. The outflowing of a jet is recognized from the interface. In the calculation, 90% of the plastic work was assumed to dissipate into heat. Since the largest extent of deformation and the highest strain rate can be found around the circled regions, the largest temperature increase is expected in this area, implying the occurrence of thermal softening and shear instability. Figure 13 shows the effect

Table 3. List of material parameters at 293 K used for simulation of single particle impact.

	Unit	Cu	Carbon steel
Density	kg cm^{-3}	8960	7870
Elastic modulus	Gpa	124	210
Specific heat	J (kg K^{-1})	383	486
Melting point	K	1356	1538
Thermal expansion coefficient	10^{-6} K^{-1}	16.5	11.6
Yield stress	MPa	90	175
Strain hardening component		0.31	0.39

For room temperature (293 K).

of particle velocity on the impact behavior of a copper particle onto a low-carbon steel substrate. The contours show a temperature distribution when the maximum deformation was observed in the jet region. As particle velocity increases, the extent of deformation at the interface increases resulting in higher chance of bonding between the particle and the substrate. Figure 14 shows the variation in the critical velocity as a function of the initial particle temperature. Here, the critical velocity was assumed to be the particle velocity at which the melting point of a particle is achieved at the interface after impact. This condition can be very close to the condition of the occurrence of shear instability. However, it should be noted that this assumption essentially tends to overestimate the critical velocity. This is because bonding due to surface adhesion does not always require the melting of the surface as discussed above, although this mechanism remains a hypothesis. The critical velocity necessary to adhere a copper particle onto a copper substrate is about 540 m s^{-1} at room temperature and decreases as the initial particle temperature increases. When the initial particle temperature reaches 973 K, the critical velocity comes down to 300 m s^{-1}. This implies that a higher particle temperature can compensate for a lower particle velocity and that the deposition of a solid particle should be easier at a higher particle temperature. These calculation results clearly point out the advantages of warm spray deposition. Figure 15 shows the effect of the particle size on the critical velocity for a titanium particle impacting on a titanium substrate. Since titanium has a higher plastic deformation resistance than copper, its estimated critical velocity is much higher than that of copper. As the particle size decreases, the critical velocity increases, which indicates that larger particles are easier to adhere on the substrate if the flying velocity is the same. However, this is not always the case. In the above particle simulation, rebounding is not taken into account for critical velocity evaluation. The rebounding probability increases with increasing elastic energy stored in the particle which is released in the form of kinetic energy of rebounding when the dynamic impact pressure ceases to act. According to Kilinkov's estimation, the ratio of the accumulated elastic energy to the adhesion energy increases in proportion to the particle size, thus in general larger particles should have a higher possibility of rebounding. In addition, in the actual spray process, smaller particles usually travel faster and larger particles fly slower. Thus, there must be appropriate and optimized process conditions for each material.

Several attempts to compare the numerical simulation and experimental results have been made. Schmidt *et al* [25] evaluated the critical velocity by spray experiments and explosive powder compaction. They calculated particle impact velocity or shock wave velocity by numerical analysis and evaluated the critical velocity for bonding on the basis of the deposition efficiency or microstructure. The estimated critical velocity for various materials showed good agreement with those experimentally determined values [25]. An attempt to correlate a single-particle impact phenomenon with numerical calculation was also made by Watanabe *et al* [27]. In their work, the deformation field of a copper particle impacted on the substrate was evaluated by the electron Moiré method, as shown in figure 16. In the figure, the white lines are Moiré fringes. The reduction in the spacing of the lines can be recognized near the particle (upper part) and the impression of rebounded particle (bottom) indicating significant in-plane tensile deformation in the vertical

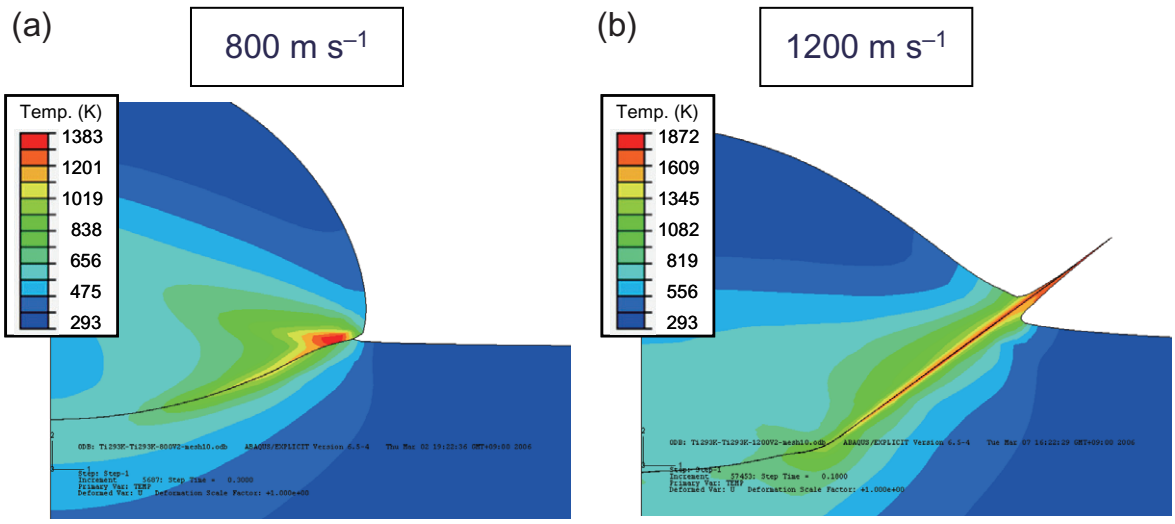

Figure 13. Effect of particle velocity on impact of copper particle onto low-carbon steel substrate.

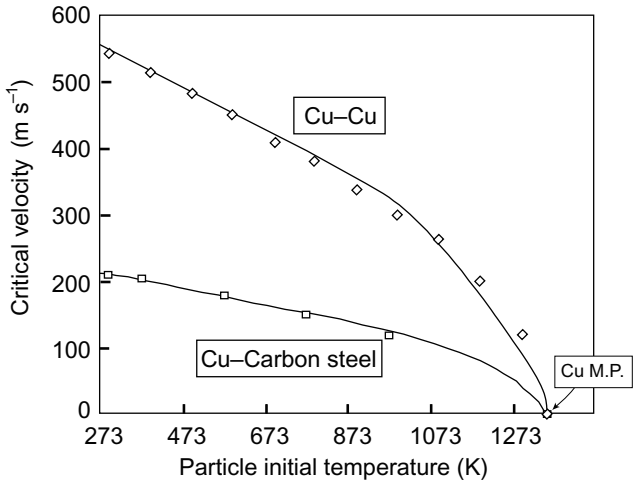

Figure 14. Variation in critical velocity as function of initial particle temperature.

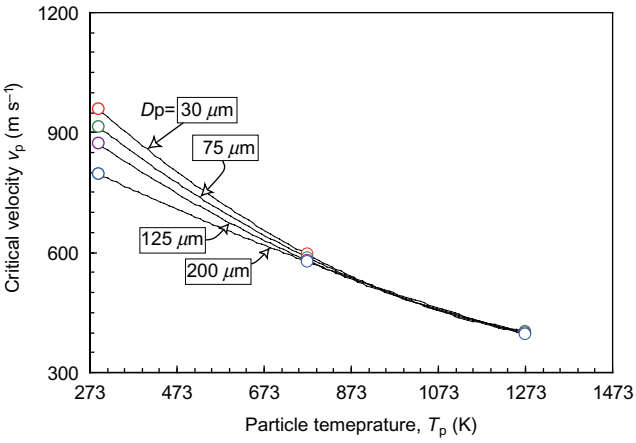

Figure 15. Effect of particle size on critical velocity for titanium particle impacting on titanium substrate.

direction of the figure. The plastic strain was evaluated from the variation in the spacing and compared with the numerically estimated values. Although there remains some ambiguity about the particle impact velocity and the initial particle temperature, the order of the estimated data shows good agreement. However, the available data are still limited and further investigations must be carried out in order to understand the bonding mechanisms and establish the optimum process conditions.

4. Emerging applications of warm spraying

4.1. Metal (Titanium)

The coating of titanium is expected to have a wide range of applications in the industry such as various components of large structures such as bridges and ships, piping and tanks in chemical plants, heat exchangers and surgical implants. This is because Ti has several attractive properties such as superb corrosion resistance, inertness in the human body, light weight, high specific strength and low paramagnetism. On the other hand, Ti is a very reactive metal at high temperatures because of its strong affinity with gases such as oxygen, nitrogen and hydrogen. Therefore, fabrication processes in the inert atmosphere, e.g. physical vapor deposition (PVD) or low-pressure plasma spraying (LPPS) have been the most promising process for forming titanium coatings with low oxygen content [28, 29].

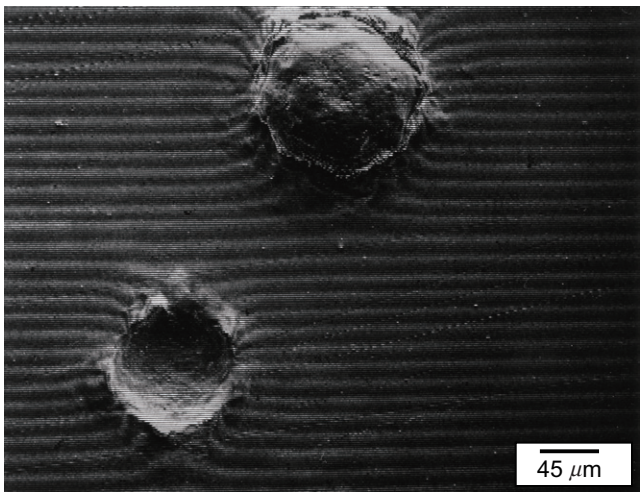

Figure 16. Deformation field of copper particle impacting on substrate evaluated by electron Moiré method.

It would be much more advantageous if it becomes possible to coat Ti in air for the following reasons: higher operation efficiency, no limitation to the size of the work, and more freedom in the fabrication site. The cold spraying of titanium powder has been reported to produce porous but essentially oxygen-free coatings and its density could be improved by post processing such as machining [30]. As has already been explained in section 2, warm spraying is capable of raising the temperature of titanium particles considerably higher compared with cold spraying, i.e. up to 1300 K, which is still considerably lower than the melting point, while keeping the velocity at approximately 800 m s^{-1}. This has lead to the successful fabrication of titanium coatings with both high packing density and high purity.

Figure 17 shows the open porosity of the coatings prepared under various spray conditions. Examples of the cross-sectional images of the coatings are shown in figure 18. The cross sections indicate that highly dense to porous coatings could be obtained. Further densification of Ti coatings was achieved by adopting a bimodal size distribution of feedstock powder. When 1 mass% large Ti particles (63–90 μm) were mixed with the conventional feedstock powder of smaller than 45 μm diameter, the coating porosity decreased from 2.3 to 0.8 vol% simultaneously with the decrease in oxygen content to 0.26 mass%, which was comparable to the level of the feedstock powder. This densification was also clearly observed in the comparison of appearance of Ti coatings formed on a steel substrate after immersion test in neutral saline solution [31]. Whereas a number of red rusts appeared on the surface of the coating formed with ordinary powder, the number of red rust particles decreased markedly with the bimodal powder.

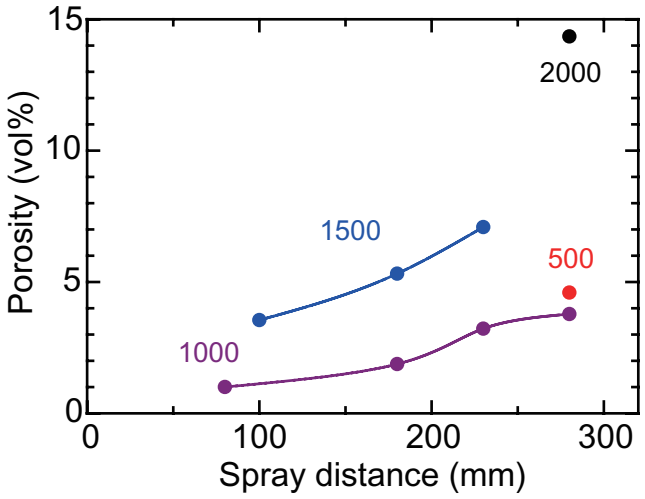

Figure 17. Open porosity of Ti coatings fabricated by warm spraying as function of spray distance. Number shows nitrogen flow rate (slm) into mixing chamber of warm spray apparatus.

As discussed in section 2, the primary chemical reaction of flight particles in warm spraying is oxidation. The oxygen content of the coatings fabricated by warm spraying was suppressed to significantly low levels in comparison with those for the coatings fabricated with other atmospheric thermal spray techniques except cold spraying, and nitrogen is expected to be taken up in the Ti coatings because the Ti feedstock powder was supplied to the hot jet containing nitrogen gas. The result of the chemical analysis, however, shows that the nitrogen content of the coatings was generally one order smaller than the oxygen content under various spraying conditions, and that it was equal even to the level of the feedstock powder under some spraying conditions.

4.2. Metallic glass [32]

Amorphous alloys have homogenous structures without grain boundaries and inclusions compared with crystalline metals of the same chemical composition owing to their random atom arrangement [33]. Because of this unique structure, amorphous alloys have excellent physical properties such as high strength, soft magnetism and high corrosion resistance. In addition to the advantages described above, Zr-based glass alloys, for example, have Young's modulus of approximately 80 GPa, which is lower than that of conventional metallic biomaterials such as 316L stainless steel, which is approximately 190 Gpa [34]. If such metallic glasses are used for bone fixation devices and artificial joints, the stress shielding to bone by the device could be reduced because human bone has a very low Young's modulus, typically approximately 20 GPa, leading to a decrease in the extent of bone absorption. Using a glass alloy as a structural material in bone fixation devices and artificial joints, where the material experiences both impact and repetitive stresses, however, might have some risks in reliability because of its insufficient toughness. This leads to a concept of using glass alloys in combination with conventional metallic biomaterials as one of the effective solutions to take advantages of

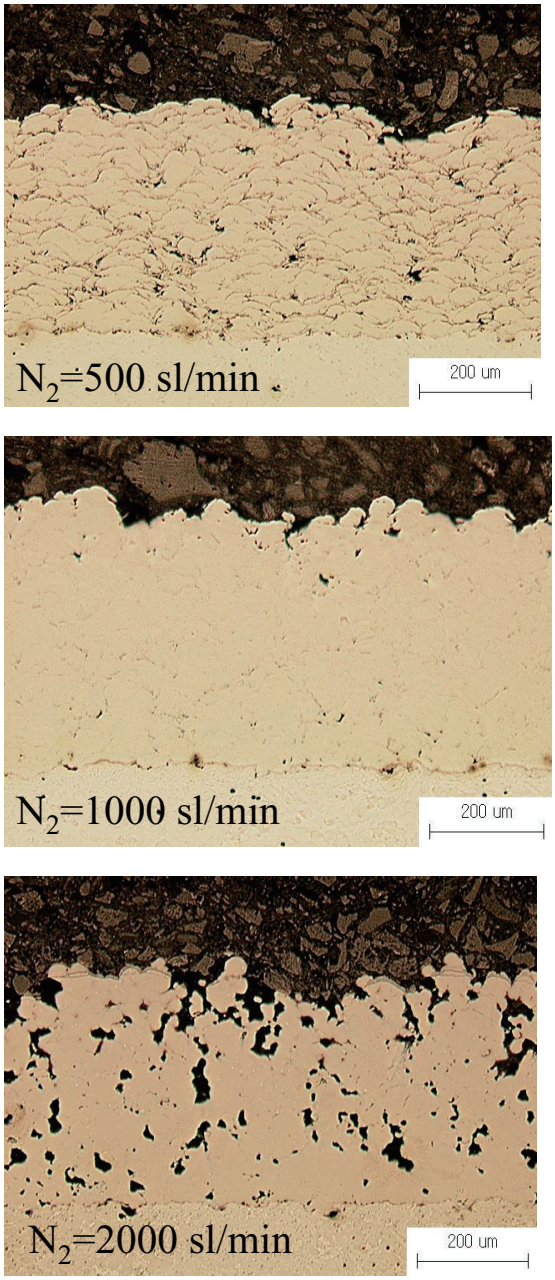

Figure 18. Cross sections of Ti coatings fabricated by warm spraying at three nitrogen flow rates.

the properties of both materials, i.e. high strength and toughness.

As techniques for bonding a glass alloy and another material, powder sintering [35], casting [36], thermal spraying [37] and other methods have been reported. In the processing of glass alloy, keeping the material's purity and amorphous structure is essential, and applicability to complicated substrate shape at high productivity is desired for industrial realization in the future. Therefore, warm spraying is expected to be a suitable technique for forming Zr-based metallic glass on a crystalline metal substrate.

The XRD patterns of Zr-based glass alloy (Zr-12.3Cu-7.6Ni-3.5Al in mass%) deposits are shown in figure 19 in comparison with that of the feedstock powder.

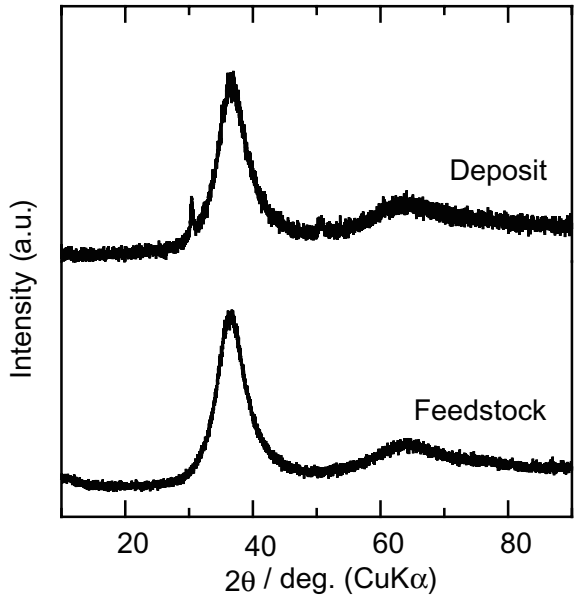

Figure 19. XRD patterns of Zr-based glass alloy deposit prepared by warm spraying on steel substrate in addition to feedstock powder.

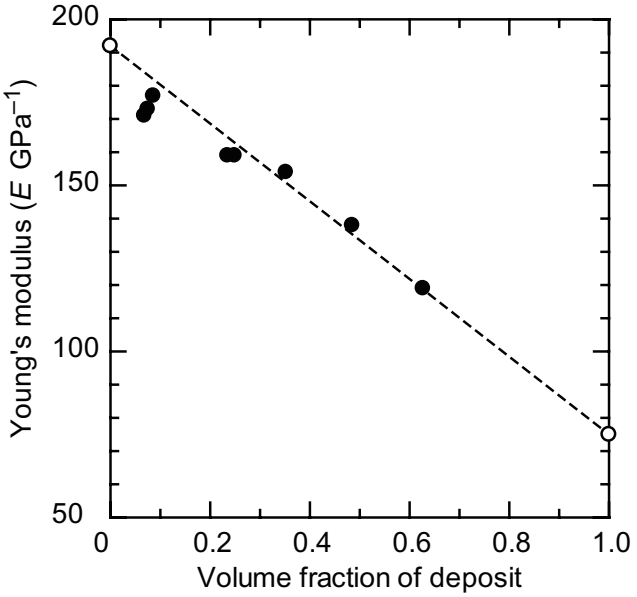

Figure 20. Relationship between Young's modulus and volume fraction of Zr-based glass alloy deposit combined with 316L stainless steel substrate. The broken line ties the values of bulk materials of 316L stainless steel and Zr-based glass alloy.

The feedstock powder was amorphous, with no obvious peaks except the hallow peak at approximately 30–40°. The deposit prepared by warm spraying shows very small peaks assigned to ZrO_2. Therefore, the deposit contained a small amount of oxide formed by oxidation during spraying, whereas the glass alloy matrix of the deposits maintained its amorphous structure. The crystallization of the Zr-based glass alloy did not take place because the temperature of in-flight particles during warm spraying was relatively low and the heating duration was as short as 1 ms. Since Zr is also a very reactive metal, the result also confirms that lowering the process temperature in warm spraying is effective for suppressing oxidation.

Figure 20 shows the relationship between the apparent Young's modulus of the composites and the volume fraction of the substrate. This figure indicates that the rule of mixture holds true for Young's modulus of the glass alloy layer/stainless steel composites fabricated by warm spraying.

4.3. WC–Co coatings fabricated by warm spraying [38, 39]

WC–Co cermet coatings have been used to enhance the wear resistance of various engineering components owing to their high hardness and moderate toughness compared with other coating materials. Thus far, high-velocity oxy-fuel (HVOF) spraying is the most suitable technique for fabricating WC–Co coatings; however, the properties of HVOF sprayed coatings are still inferior to those of sintered bulk materials. For example, although the fracture toughnesses of as-sprayed WC-Co coatings are about 3–5 $MPam^{1/2}$, those of the bulk material are 15–30 $MPam^{1/2}$, depending on the volume fraction of the binder phase. HVOF-sprayed WC–Co coating suffers from high temperature, leading to the decarburization and dissolution of carbides during deposition and resulting in the formation of brittle W_2C and Co–W–C(η) phases. By applying warm spraying to the deposition of WC–Co, it is expected to fabricate cermet coatings without detrimental phases such as W_2C and η phases, and to develop new cermet coatings with similar microstructures and mechanical properties to sintered bulk hard metals.

A backscattered electron (BSE) image of a WC–Co splat deposited by warm spraying is shown in figure 21. A splat image of conventional HVOF spraying is also shown for comparison. Although the HVOF splat indicates melting during flight, the warm-sprayed splat shows a blocky microstructure of carbides with no sign of melting, implying the occurrence of solid particle impacts. By applying warm spraying, a coating with a thickness of ~150 μm was successfully fabricated (figure 22). The coating microstructure was dense and contained a substantially higher amount of WC than conventional HVOF-sprayed coatings implying the less detrimental reactions of WC such as decarburization and dissolution in to the binder phase during the process. Figure 23 shows XRD patterns of the powder and coating. The original powder consisted of WC and Co. Although the broadening of Co peaks can be observed at approximately 43°, the fabricated coating also shows only WC and Co peaks. Thus, it can be said that the deposited coatings are essentially degradation-free coatings, which are quite promising. The hardnesses of the coatings were about 1300 Hv, similar to those of sintered bulk material and HVOF coatings. The correlations among spray conditions, microstructure and mechanical performance are under investigation.

4.4. Oxides [40, 41, 42]

Oxides, particularly transition-metal oxides are of special interests because of their catalytic function and electron storage function. The reaction rate of these functions depends

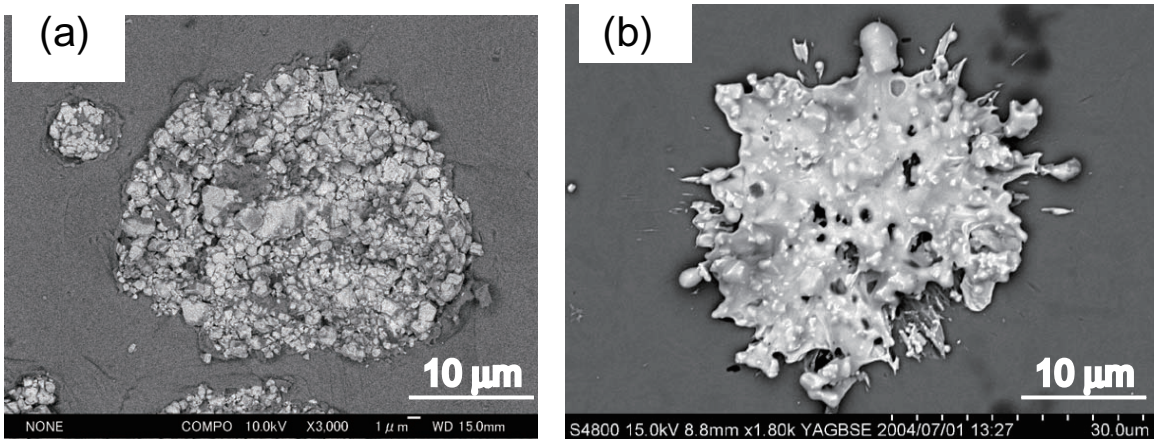

Figure 21. BSE images of splats deposited by (a) HVOF and(b) warm spraying.

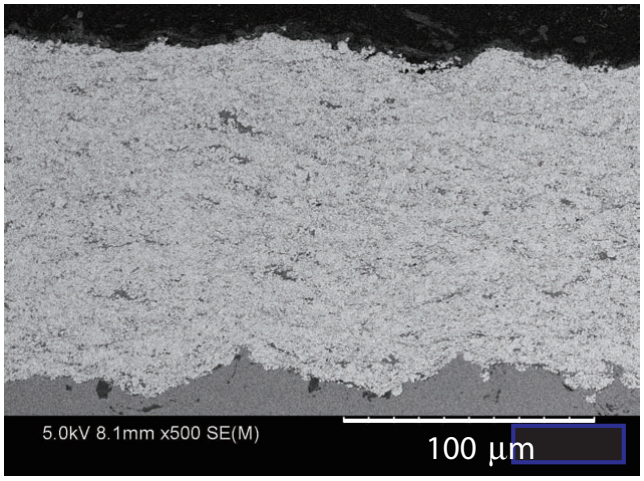

Figure 22. Polished cross section (SE image) of WC-Co coating deposited by warm spraying.

on surface area and can be improved by the quantum size effect [43]. It is highly beneficial to fabricate nanosized transition-metal oxides on a suitable substrate in various applications.

For the industrial development of deposition processes for transition-metal oxides such as TiO_2, processes using a liquid solution such as painting technology as well as electrodeposition have been applied [44, 45, 46]. However, problems with residues of binders, inevitable post heat treatment, and low adhesion and cohesion of the coatings remain, even if their capability for high-speed deposition to a large surface area is taken into account. Alternately, although conventional thermal spraying technology has been applied, the thermal deterioration of TiO_2 such as phase transformation and particle growth could not be controlled completely [47, 48].

Coatings of TiO_2 and Fe_2O_3 as transition-metal oxides of nanosize were fabricated by warm spraying. TiO_2 is well known for its photoelectrochemical function, e.g. as a photocatalyst. Transition-metal oxides such as Fe_2O_3, WO_3 and SnO_2 can be used as electron storage materials. By putting these materials in one device, solar energy can be converted to electric power and used effectively 24 h a day. One example is the continuous photocathodic protection of steel structures from corrosion [49, 50]. During daytime, the photoelectrochemical function makes the electrode potential less noble, exerting cathodic protection of the metal substrate and charge electrons into storage. During nighttime, electrons in storage are discharged to the substrate to sustain the cathodic protection function.

Figure 24 shows an SEM image of the coating obtained by warm spraying, showing particles similar to the feedstock powder particles. Therefore, the thermal growth of primary composite particles and their melting were prevented during coating. XRD analysis revealed that the coatings prepared by warm spraying consist of the same crystalline phases such as the anatase phase of TiO_2 and the hematite phase of Fe_2O_3. These results indicate that the thermal deterioration of feedstock materials, which is inevitable in conventional thermal spraying, is suppressed effectively.

Figure 25 shows polarization curves of the above-mentioned composite coatings. The current recorded was obtained under UV illumination of the surface of TiO_2–Fe_2O_3 coatings and thus termed photocurrent. The two coatings prepared by warm spraying generally had larger photocurrents in the potential range tested than that prepared by commercial HVOF spraying as a reference. In addition, the electron charge/discharge function of the Fe_2O_3 of the TiO_2–Fe_2O_3 coatings was evaluated. Similarly, the warm-sprayed coating with the finest grains performed best. In other words, the suppression of thermal deterioration and the increase in the primary particle size of the coatings improved the electron charge/discharge characteristics. These electrochemical characteristics of the coatings show the possibility of realizing full-time photocathodic protection coatings.

4.5. Plastics

For plastic coatings applied by thermal spraying in the industry, thermoplastic resins with comparatively high fluidity such as polyethylene, poly(ethylene vinyl acetate, EVA) and nylon 11 as well as thermosetting resins such as epoxy

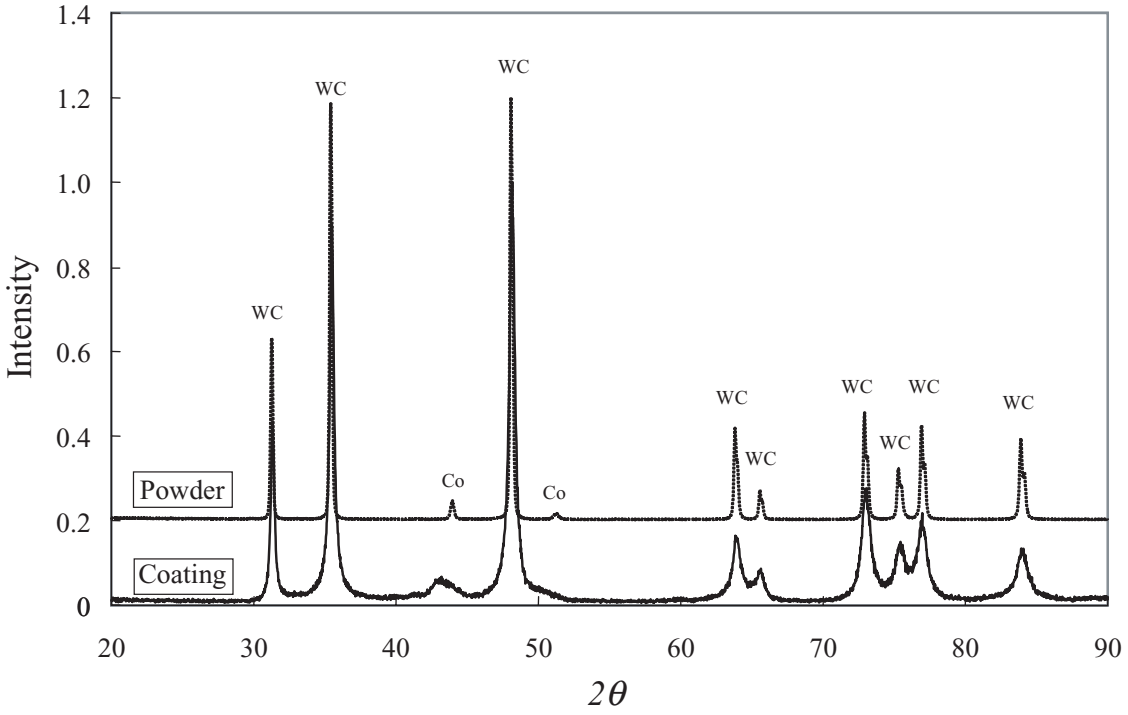

Figure 23. XRD patterns of original powder and coating of WC-12 mass% Co fabricated by warm spraying.

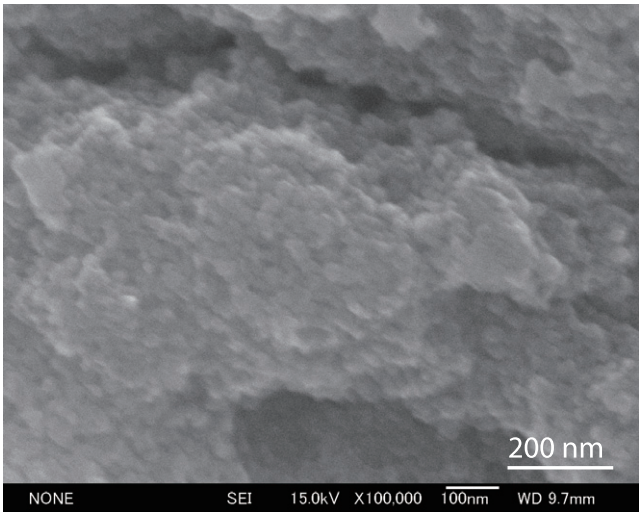

Figure 24. SEM image of surface of TiO_2–Fe_2O_3 coating fabricated by warm spraying.

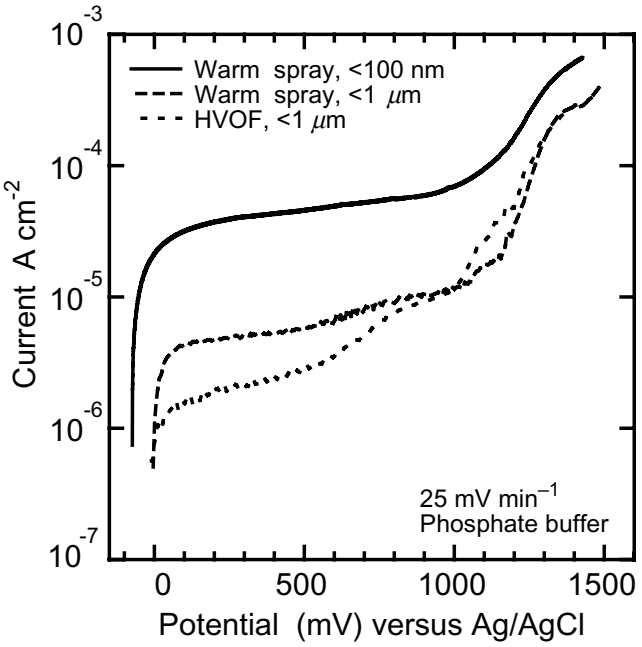

Figure 25. Polarization curves under UV illumination of TiO_2–Fe_2O_3 coatings with different fabrication processes and particle sizes.

resin, which are cured by heating after spraying, have been used. The basic demand to develop such plastic spraying comes from the fact that the application of conventional powder coatings to target surfaces with complicated shapes is difficult and thermal spraying can provide on-site application capability.

Fundamental studies of thermally sprayed plastic coatings have been carried out using the above-mentioned materials, which aim to clarify the particle deposition mechanism [51, 52] and relate it to coating performance such as wear resistance [53]. To improve adhesion between a plastic coating and a substrate, polymers and copolymers with functional groups were investigated, e.g. poly(ethylene-co-vinyl alcohol) [54], modified poly(ethylene) [55, 56] and ethylene methacrylic acid (EMAA) [57, 58]. Composite coatings of polymers and inorganic materials such as WC/Co [59] and hydroxyapatite [60] were fabricated to enhance tribological properties and biological activity, respectively.

A challenge in the thermal spraying of plastics lies in materials with low fluidity. This class of plastics is not applicable to conventional powder coating processes. Poly(ether ether ketone) (PEEK) is one of such engineering plastics with low fluidity possessing highly attractive properties, which is expected to replace steel for some components in the automotive industry. There have been several reports on the thermal spraying of PEEK. Coating characteristics such as chemical bonding and crystallinity are related to the process conditions during coating fabrication [61, 62]. Coating properties such as wear resistance and corrosion resistance were also investigated [63, 64]. As is often the case with thermally sprayed coatings, however, the thermal degradation of PEEK such as chemical change and amorphization take place with an increase in spraying temperature while an insufficient melting of PEEK leaves many pores in the coatings with lower spray temperatures [65, 66]. Therefore, the post-spray heat treatment of PEEK coatings prepared at low spraying temperature, has been investigated [65, 66].

The spraying of ultrahigh-molecular-weight polyethylene (UHMWPE) has been studied by the authors because even though UHMWPE is known for its superb mechanical and physical properties such as high strength, low friction coefficient, nonstick surface, and high corrosion resistance in acids, it has been almost impossible to attain coatings of UHMWPE by thermal spraying owing to its low fluidity. In addition, it is much less expensive than PEEK. In a report on the thermal spraying of UHMWPE, sprayed coatings were reported to become more brittle owing to thermal degradation in the process [67]. Recently, by carefully tuning warm spraying parameters, the fabrication of smooth and dense coatings of UHMWPE with a thickness of up to 100 μm has become possible [68]. The FTIR spectra as well as the color of the obtained coatings show little sign of degradation. Even at 50 μm thickness, the coating showed a good corrosion protection for steel substrates in seawater.

5. Summary

A review of a novel spray process called warm spraying (2-stage HVOF) developed at NIMS was given. In this process, coatings were made by successive impacts of powder particles, which were heated to an appropriate temperature below the melting point and accelerated to a high velocity beyond the critical velocity for bonding formation. The basic principles of the spray equipment and the fundamental processes were described such as the gas dynamics of particle heating and acceleration, the oxidation of titanium particles during warm spraying, and the high-velocity impact phenomena of solid particles. Finally, examples of emerging applications such as coatings of titanium, metallic glass, cermet and plastics were described briefly. Because of its capability to control the temperature of sprayed particles in a wide range, warm spraying fills the gap between HVOF and cold sprayings in the processing window of thermal spray processes.

Acknowledgments

We are thankful to Mr Kensuke Yokoyama and Mr Tommy Wu in performing the numerical simulations of particle impact and the in-flight oxidation, respectively, and Dr Pornthep Chivavibul for his pioneering investigation on warm spraying of cermets. We are also grateful to Mr Masayuki Komatsu and Mr Nobuyuki Kakeya for the operation and maintenance of the warm spraying equipment. This work was partially supported by KAKENHI 19360335.

References

[1] Pawlowsiki L 1995 *The Science and Technology of Thermal Spray Coatings* (New York: Wiley)
[2] Papyrin A, Kosarev V, Klinkov S, Alkhimov A and Fomin V 2007 *Cold Spray Technology* (Oxford: Elsevier)
[3] Schmidt T, Gaertner F and Kreye H 2006 *J. Therm. Spray Technol.* **15** 488
[4] Katanoda H 2006 *Mater. Trans.* **47** 2791
[5] Zucrow M J and Hoffman J D 1976 *Gas Dynamics* (New York: John Wiley) p 41
[6] Katanoda H, Fukuhara M, Iino N and Matsuo Yousha K 2007 *J. Japan Therm. Spraying Soc.* **44** 1 (in Japanese)
[7] Tam C K W, Jackson J A and Seiner J M 1985 *J. Fluid Mech.* **153** 123
[8] Witze P O 1974 *AIAA J.* **12** 417
[9] Wu T, Kuroda S, Kawakita J, Katanoda H and Reed R 2006 *Proc. Int. Thermal Spray Conf.* (ASM International) CD-ROM
[10] Guillen D P and Williams B G 2006 *J. Therm. Spray Technol.* **15** 63
[11] Zhang H W, Vardelle A and Themelis N J 2003 *High Temp. Mater. Process.* **7** 277
[12] Hurlen T 1960–61 Oxidation of Titanium *J. Inst. Metals* **89** 128
[13] Kofstad P *High-Temperature Oxidation of Metals* (New York: Wiley) p 169
[14] Klinkov S V, Kosarev V F and Rein M 2005 *Aerosp. Sci. Technol.* **9** 582
[15] Gilmore D L, Dykhuizen R C, Neiser R A, Roemer T J and Smith M F 1999 *J. Therm. Spray Technol.* **8** 576
[16] Van Steenkiste T H, Smith J R and Teets R E 2002 *Surf. Coat. Technol.* **154** 237
[17] Stoltenhoff T, Kreye H and Richter H J 2002 *J. Therm. Spray Technol.* **11** 542
[18] Assadi H, Gärtner F, Stoltenhoff T and Kreye H 2003 *Acta Mater.* **51** 4379
[19] Li C J, Li W Y and Liao H L 2006 *J. Therm. Spray Technol.* **15** 212
[20] Grujicic M, Saylor J R, Beasley D E, DeRosset W S and Helfritch D 2003 *Appl. Surf. Sci.* **219** 211
[21] Papyrin A, Kosarev V, Klinkov S, Alkhimov A and Fomin V 2007 *Cold Spray Technology* (Oxford: Elsevier)
[22] Li W Y, Zhang C, Wang H T, Guo X P, Liao H L, Li C J and Coddet C 2007 *Appl. Surf. Sci.* **253** 3557
[23] Morizono Y, Muto M, Nihsida M, Asada T, Yamamuro T and Chiba A 2005 *Quaterly J. Japan Weld. Soc.* **23** 296
[24] Borchers C, Gartner F, Stoltenhoff T, Assadi H and Kreye H 2003 *J. Appl. Phys.* **93** 10064
[25] Schmidt T, Gärtner F, Assadi H and Kreye H 2006 *Acta Mater.* **54** 729
[26] Yokoyama K, Watanabe M, Kuroda S, Gotoh Y, Schmidt T and Gärtner F 2006 *Mater. Trans.* **47** 1697
[27] Watanabe M, Kishimoto S, Xing Y, Shinoda K and Kuroda S 2007 *J. Therm. Spray Technol.* **16** 940

[28] Khelfaoui Y, Kerlar M, Bali A and Dalard F 2006 *Surf. Coat Technol.* **200** 4523
[29] Steffens H D, Erturk E and Busse K H 1985 *J. Vac. Sci. Technol.* A **3** 2459
[30] Karthikeyan J, Kay C M, Lindeman J, Lima R S and Berndt C C 2000 *Thermal Spray: Surface Engineering via Applied Research* ed C C Berndt (Montréal, Québec Canada: ASM International) p 255
[31] Kawakita J, Watanabe M, Kuroda S and Katanoda H 2007 *Proc. Int. Therm. Spray Conf. ASM International* p 43
[32] Kawakita J, Maruyama N, Kuroda1 S, Hiromoto S and Yamamoto A 2008 *Mater. Trans.* **49** 317
[33] Klement W J, Willens R H and Duwez P 1960 *Nature* **187** 869
[34] Inoue A 1999 *Bulk Amorphous Alloys—Practical Characteristics and Applications—Materials Science Foundations* vol 6 (Switzerland: Trans. Technol. Publications, Zürich) p 1
[35] Lee J K, Kim H J, Yamasaki M, Kawamura Y and Bae J C 2005 *Mater. Sci. Forum* **475–479** 3419
[36] Shen J, Zou J, Ye L, Lu Z P, Xing D W, Yan M and Sun J F 2005 *J. Non-Crystal. Solids* **351** 2519
[37] Kim H J, Lim K M, Seong B G and Park C G 2001 *J. Mater. Sci.* **36** 49
[38] Chivavibul P, Watanabe M, Kuroda S and Shinoda K 2007 *Surf. Coat. Technol.* **202** 509
[39] Watanabe M, Pornthep C, Kuroda S, Kawakita J, Kitamura J and Sato K 2007 *J. Japan Inst. Metals* **71** 853 (in Japanese)
[40] Kawakita J, Shinohara T, Kuroda S, Suzuki M and Sodeoka S 2007 *Proc. Eurocorrosion* CD-ROM
[41] Kawakita J, Shinohara T, Kuroda S, Suzuki M and Sodeoka S 2008 *Surf. Coat. Technol.* **202** 4028
[42] Onizawa K, Kawakita J, Kuroda S, Shinohara T, Suzuki M, Sodeoka S and Sakamoto Y 2008 *J. Solid Mech. Mater. Eng.* **2** 156
[43] Hua Z, Shi J, Zhang L, Ruan M and Yan J 2002 *Adv. Mater.* **14** 830
[44] Sarkar P and Nicholson P S 1996 *J. Am. Ceram. Soc.* **79** 1987
[45] Negishi N and Takeuchi K 2001 *Thin Solid Films* **392** 249
[46] Gómez M M, Lu J and Olsson E 2000 *Sol. Energy Mater. Sol. Cells* **64** 385
[47] Ohmori A, Shoyama H, Matsuoka S, Ohashi K, Moriya K and Li C 2000 *Thermal Spray: Surface Engineering via Applied Reasearch* ed C C Berndt (Materials Park, OH: ASM International) p 317
[48] Lee C, Choi H, Lee C and Kim H 2003 *Surf. Coat. Technol.* **173** 192
[49] Ohko Y, Tatsuma T and Fujishima A 2001 *J. Electrochem. Soc.* **148** B24
[50] Subasri R and Shinohara T 2003 *Electrochem. Commun.* **5** 897
[51] Ivosevic M, Gupta V, Baldoni J A, Cairncross R A, Twardowski T E and Knight R 2006 *J. Therm. Spray Technol.* **15** 725
[52] Ivosevic M, Cairncross R A and Knight R 2006 *Int. J. Heat Mass Transfer* **49** 3285
[53] Niebuhr D and Scholl M 2005 *J. Therm. Spray Technol.* **14** 487
[54] Oksuz M and Yildirim H 2004 *J. Appl. Polym. Sci.* **94** 1357
[55] Sugama T, Kawase R, Berndt C C and Herman H 1995 *Prog. Org. Coat.* **25** 205
[56] Branco J R T, Campos S R V, Duarte L T and Lins V 2004 *J. Appl. Polym. Sci.* **92** 3159
[57] Lins V F C, Branco J R T, Diniz F R C, Brogan J C and Berndt C C 2007 *Wear* **262** 274
[58] Yan F Y, Gross K A, Simon G P and Berndt C C 2003 *J. Appl. Polym. Sci.* **88** 214
[59] Ivosevic M, Knight R, Kalidindi S R, Palmese G R and Sutter J K 2006 *Surf. Coat. Technol.* **200** 5145
[60] Sun L M, Berndt C C and Gross K A 2002 *J. Biomater. Sci. Polym. Ed.* **13** 977
[61] Simonin L and Liao H 2000 *Macromol. Mater. Eng.* **283** 153
[62] Strait L H and Jamison R D 1994 *J. Compos. Mater.* **28** 211
[63] Li J F, Liao H L and Coddet C 2002 *Wear* **252** 824
[64] Normand B, Takenouti H, Keddam M, Liao H, Monteil G and Coddet C 2004 *Electrochim. Acta* **49** 2981
[65] Zhang G, Liao H, Yu H, Costil S, Mhaisalkar S G, Bordes J M and Coddet C 2006 *Surf. Coat. Technol.* **201** 243
[66] Zhang G, Liao H, Yu H, Ji V, Huang W, Mhaisalkar S G and Coddet C 2006 *Surf. Coat. Technol.* **200** 6690
[67] Bao Y, Zhang T and Gawne D T 2005 *J. Mater. Sci.* **40** 77
[68] Kawakita J 2007 *Proc. Fall Meet. Japan Therm. Spray Soc.* pp 55–6 (in Japanese)